CRYSTAL GROWTH & DESIGN

pubs.acs.org/crystal Article

High-Throughput Screening, Crystal Structure Prediction, and Carrier Mobility Calculations of Organic Molecular Semiconductors as Hole Transport Layer Materials in Perovskite Solar Cells

Md Omar Faruque, Suchona Akter, Dil K. Limbu, Kathleen V. Kilway, Zhonghua Peng,* and Mohammad R. Momeni*

Cite This: *Cryst. Growth Des.* 2024, 24, 8950−8960 Read Online

ACCESS | Metrics & More | Article Recommendations | Supporting Information

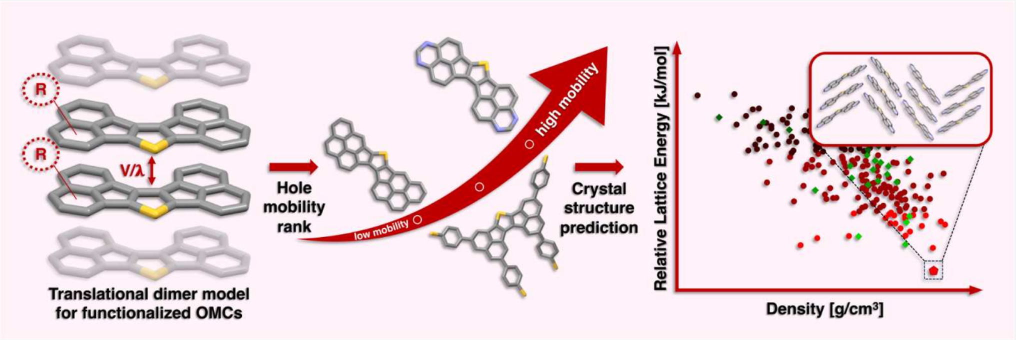

ABSTRACT: Using a representative translational dimer model, high throughput calculations are implemented for fast screening of a total of 74 diacenaphtho-extended heterocycle (DAH) derivatives as hole transport layer (HTL) materials in perovskite solar cells (PVSCs). Different electronic properties, including band structures, band gaps, and band edges compared to methylammonium and formamidinium lead iodide perovskites, along with reorganization energies, electronic couplings, and hole mobilities are calculated in order to decipher the effects of different parameters, including the polarity, steric and π-conjugation, as well as the presence of explicit hydrogen bond interactions on the computed carrier mobilities of the studied materials. Full crystal structure predictions and hole mobility calculations of the top candidates resulted in some mobilities exceeding 10 $cm^2/V \cdot s$, further validating the employed translational dimer model as a robust approach for inverse design and fast high-throughput screening of new HTL organic semiconductors with superior properties. The studied models and simulations performed in this work are instructive in designing next-generation HTL materials for higher-performance PVSCs.

1. INTRODUCTION

Perovskite solar cells (PVSCs) are among the most exciting and promising new solar cell technologies hailed as the future of solar power.[1−9] The first PVSC was reported in 2009 with a power conversion efficiency (PCE) lower than 4%.[1] Since then, the efficiency of PVSCs has skyrocketed to over 25%,[10] surpassing multicrystalline Si-based solar cells, making them the most appealing new technology for solar-electricity conversion.[11] A typical PVSC is comprised of a central light-absorbing perovskite layer sandwiched with two electrodes, a cathode and an anode, which collect photogenerated electrons and holes, respectively, from the perovskite. To facilitate unidirectional charge transfer and collection, an electron-transporting layer (ETL) is introduced between the perovskite and the cathode, while a hole-transporting layer (HTL) is inserted between the perovskite and the anode.

The HTL plays a critical role in device performance in terms of both its efficiency and long-term stability.[12−17] Some of the most important properties of an ideal HTL material include (1) high intrinsic hole mobility (>10^{-2} $cm^2/V \cdot s$) without the need for any doping; (2) good valence and conduction band alignments with perovskites; (3) high chemical, thermal, and photostability; and (4) low cost with convenient synthesis from readily available source materials.[12−18] Despite advances in the development of a variety of HTL materials, 2,2′,7,7′-tetrakis(*N*,*N*-di-*p*-methoxyphenylamine)-9,9′-spirobifluorene (spiro-MeOTAD) remains the HTL of choice with the best-reported performances.[10,19−21] Yet, spiro-MeOTAD is expensive and is a poor conductor with low hole mobility (≈10^{-5} $cm^2/V \cdot s$) and thus requires a complicated doping process that

Received: July 11, 2024
Revised: October 8, 2024
Accepted: October 8, 2024
Published: October 16, 2024

https://doi.org/10.1021/acs.cgd.4c00965
Cryst. Growth Des. 2024, 24, 8950−8960

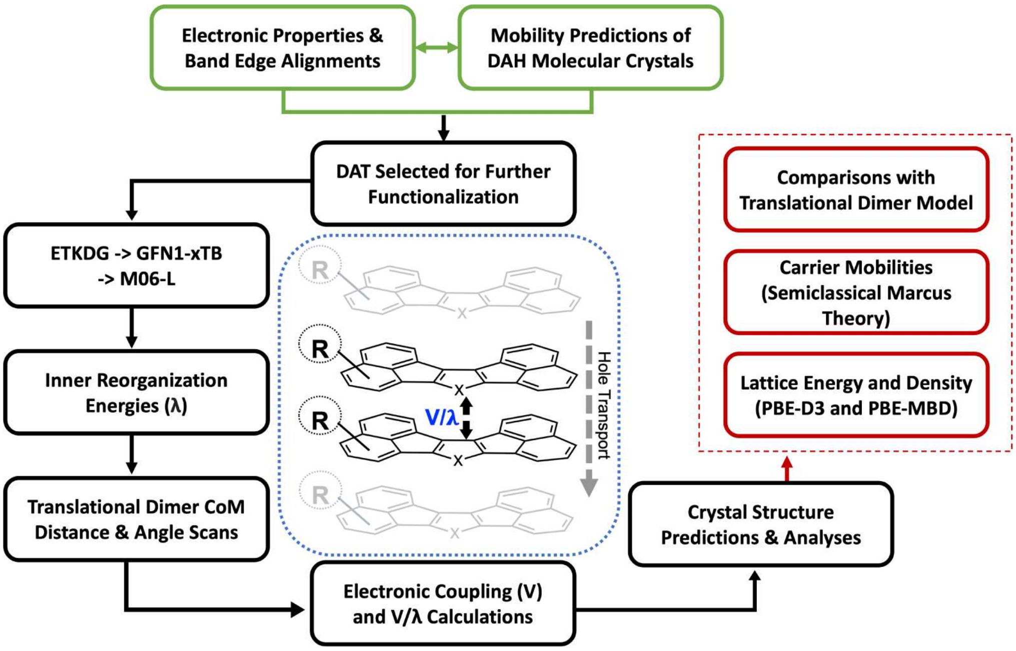

Figure 1. High-throughput screening workflow adapted in this work using the translational dimer model. All modified DAT systems (X = S) with different functional groups (R) attached in symmetric peripheral positions are screened using the ratios of the electronic coupling over reorganization energy (i.e., V/λ). For the dimers with the highest V/λ values, crystal structures are predicted with their mobilities calculated using the semiclassical Marcus theory. The main direction of carrier transport is shown in the middle panel (dotted arrow) with X = NPh and SiPh$_2$ for DAP and DAS, respectively. The complete list of all functional groups is given in Figures S8 and S9.

is difficult to control.[20] The dopants are often ions (Li-TFSI, Na-TFSI, Ag-TFSI, etc.) that attract moisture, degrading the perovskite layer.[20] Realizing that PVSCs with spiro-MeOTAD as the HTL will not be commercially viable, there have been tremendous research efforts devoted to developing new HTL materials.[18,20−23] While inorganic HTLs have also been explored,[23] they often react with the perovskite and the electrode, compromising device stability.[19]

On the other end of alternative HTL materials are organic molecular crystals (OMCs) with rigid, planar, or near planar, π-conjugated cores.[24−26] OMCs with high intrinsic carrier mobilities have made themselves indispensable not only to PVSCs, the focus of the current study, but also to other applications in electronics and photonics, including organic field-effect transistors[27,28] as well as organic light-emitting diodes[29] and organic photovoltaics,[30] among others. In all the above-mentioned applications, high carrier mobility OMCs are essential for realizing high-performance devices. Overall, high charge carrier mobilities in OMCs can arise when long-range order is achieved through intermolecular π-stacking of the rigid core, forming columnar structures. However, typical OMCs such as tetracene and pentacene can be easily oxidized in air to form endoperoxides[31] or undergo dimerization, especially under radiation.[32,33] Here, our theoretical calculations are focused on diacenaphtho-extended [1,2-b:1′,2′-d] heterocycles (DAHs) which can potentially satisfy all above-mentioned properties for HTLs. Specifically, DAHs have a planar rigid core with π-extension much longer in one direction, similar to acenes. All aromatic rings are angularly fused, giving the system high chemical, thermal, and photostability. Moreover, the central heterocycle introduces polarity into the π system, which may increase the cofacial $\pi-\pi$ stacking interactions. All these features point to possible strong $\pi-\pi$ stacking among DAH cores with limited rotational freedom, leading to a high charge carrier mobility. When the central heterocycle is a thiophene ring, the corresponding DAT core can be conveniently synthesized in one straightforward step from the readily available inexpensive acenaphthene,[24−26,34] which distinguishes it from the complicated multistep synthesis of nearly all other OMCs with a similar number of sp^2 carbon atoms. Similarly, having 1-phenyl-1*H*-pyrrole and 1,1-diphenyl-1-*H*-silole as the central heterocycle, one can obtain the corresponding DAP and DAS core structures, respectively (see Figure 1).

In this work, we aim to not only perform high-throughput screening calculations for potential DAH-based OMCs but also to provide fundamental new insights into structure−property relationships in these materials, for example, by probing the effects of molecular packing on the calculated electronic couplings and carrier mobilities, among others. First, the electronic properties and hole mobilities of DAT, DAP, and DAS core materials as potential HTL materials are calculated using their experimentally reported crystal structures.[35,36] Specifically, density functional theory (DFT) calculated electronic band structures, band gaps, and band edges, along with reorganization energies, electronic couplings, and hole mobilities, are used to establish trends and provide fundamental understandings of charge carrier mobilities in these materials. After initial screening of the considered DAH cores, DAT is selected for systematic functionalization, with its mobilities screened by utilizing a translational dimer model as an efficient proxy. This initial screening resulted in several structures with superior hole mobilities compared to parent DAT. To design novel organic semiconductors with desired properties, the solid-state packing of the potential candidates must be predicted. Extensive theoretical research is being conducted to search the infinitely vast chemical space of potential OMCs with high carrier mobilities using a combination of crystal structure predictions (CSPs) and hole

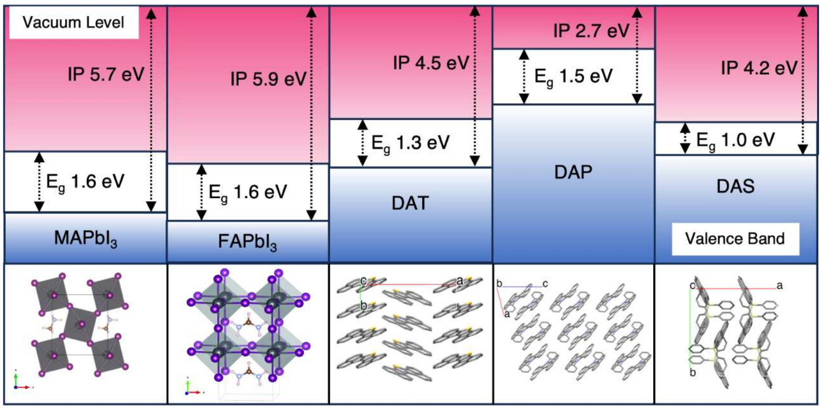

Figure 2. PBE-D3 calculated vacuum-aligned band edges of DAT, DAP, and DAS compared to MAPbI$_3$ and FAPbI$_3$ perovskites. Computed band gaps (E_g in eV) and ionization potentials (IPs in eV) are also given.

mobility calculations.[37−45] For CSP, we implemented an effective workflow leveraging machine learning (see Figure 1 for the details of our employed approach). The mobilities of the predicted crystal structures are then calculated and compared to those obtained via the adapted translational dimer approach. This work is structured as follows: our theory details are presented in the next section, Section 3 contains the results and their corresponding discussions, followed by conclusions and future outlooks.

2. MODELS AND SIMULATION DETAILS

2.1. Periodic Electronic Structure Calculations. The experimental crystal structures of DAT (CSD# 218990) and DAP (CSD# 842076) core systems were obtained from the Cambridge structural database (CSD) and were used as is, while in the case of DAS (CSD# 842077), a full CSP was performed as described in Section 2.4.[35,36] This approach was taken for the latter system as its experimentally reported crystal structure contains solvent (*n*-hexane) molecules that can affect the packing of the DAS molecules. The correlation plot between the relative lattice energy and density of the predicted structures is shown in Figure S1. A detailed comparison of the experimental crystal structure of DAS after solvent removal (four per unit cell) and full minimization with the structure obtained from our CSP is given in Figure S2. Our calculated hole mobilities for the two crystal structures show that they have similar hole transport properties: 0.20 cm^2/V·s for our CSP structure vs 0.16 cm^2/V·s for the minimized experimental structure after solvent removal (Figure S2). All structure minimizations and electronic property calculations were performed using the Vienna *ab initio* simulation package—VASP.[46−49]

First, a careful benchmark of minimized atomic positions and cell vectors was performed, without imposing any constraints, using different exchange-correlation functionals starting from the widely employed Perdew—Burke—Ernzenhof (PBE)[50] functional as well as the revised PBE (RPBE),[51] and PBE for solids (PBEsol).[52] Organic molecules in all studied solid-state crystals are π-stacked via van der Waals interactions, and hence, the correct description of these interactions is of utmost importance. Therefore, a series of dispersion correction schemes in the form of PBE functional with Becke-Johnson and zero-damped D3 dispersion correction,[53] Tkatchenko—Scheffler (PBE-TS),[54] and many-body dispersion (PBE-MBD)[55,56] schemes were employed. The results of these benchmarks are provided in Table S1. Expectedly, all pure local GGA functionals with no dispersion corrections were found to grossly overestimate the cell vectors and the CoM distances due to not accounting for these interactions. Adding Grimme's zero-damped D3 dispersion correction[53] to the PBE functional resulted in structural data that closely matched those of experiments. Therefore, PBE-D3 with zero-damping (PBE-D3 hereafter) was used throughout this work unless otherwise stated.

Interactions between electrons and ions were described by Projector Augmented Wave (PAW) potentials[57,58] with the energy cutoff of 500 eV. Gaussian smearing was adopted in all atomic position and cell vector minimizations, as well as band structure calculations with a smearing width of 0.05 eV, while the tetrahedron method was used for the calculated projected density of states (pDOS).[59] The convergence criteria were set to 10^{-5} for SCF calculations and 10^{-6} for electronic property calculations. The *k*-point mesh in the Monkhorst—Pack scheme was set to 2 × 6 × 1, 4 × 3 × 3, and 1 × 3 × 1 in the SCF part for DAT, DAP, and DAS, respectively and twice denser in the following electronic property calculations; see Figure S3 for the *k*-point paths. Spin-polarized calculations were performed for all core systems, and it was verified that all three core structures were in low spin states with all electrons paired. The PBE-D3 calculated band structures and pDOSs of all studied systems are given in Figure S4.

Vacuum-aligned band edges were calculated according to the method proposed in ref. 60 for all studied core DAHs compared to two of the most widely used perovskites: methylammonium lead iodide (MAPbI$_3$) and formamidinium lead iodide (FAPbI$_3$); see Figures 2 and S6. Briefly, slabs were generated for all systems with at least 15 Å of vacuum in the direction that is normal to the slab surface. After a ground state PBE-D3 calculation with VASP, the vacuum potentials were calculated for each of the considered systems. The vacuum potentials were aligned to a common vacuum level at 0 V, and the ionization potentials (IP) were calculated as

$$\mathrm{IP} = E_{\mathrm{VAC}} - E_{\mathrm{F}} \tag{1}$$

where E_{VAC} and E_{F} are the vacuum potential and Fermi energy, respectively.

2.2. Hole Mobility Calculations. Information about charge mobility and its relation with different packing motifs can provide important design guidelines. The standard semiclassical Marcus theory represents an excellent tool for studying carrier mobility in solid-state molecular crystals with its practical applications shown by Deng and Goddard for similar organic semiconductor crystals based on oligoacenes.[42] According to this theory, one can estimate carrier mobility rates (W_i) between near neighbor units as

$$W_i = \frac{|V_i|^2}{\hbar}\sqrt{\frac{\pi}{\lambda k_B T}}\exp\left(-\frac{\lambda}{4k_B T}\right) \tag{2}$$

where k_B and T are the Boltzmann constant and temperature (300 K), $|V_i|$ represents electronic couplings between a representative central unit with its near neighbors in the crystal (see Figure S5), and the decaying exponential corresponds to the energy barrier for the charge transport between two consecutive units which is dominated by $\lambda_{+/-}$ (the cationic/anionic reorganization energy corresponding to the transport of hole/electron, respectively). Similar to our previous study on π-stacked layered MOFs,[61] the λ term was calculated using the standard four-point scheme and molecular monomers at the M06-2X/cc-pVTZ//M06L/cc-pVTZ level of theory in Gaussian 16.[62] To ensure accuracy, we performed benchmarks on similar oligoacenes with available reference data. For example, our M06-2X/cc-pVTZ//M06L/cc-pVTZ calculated λ_+ values of 0.120 eV for tetracene and 0.101 eV for pentacene agree very well with their corresponding experimentally deduced values of 0.118 and 0.099 eV.[63] Electronic coupling, which expresses the ease of charge transfer between two neighboring units, is well-known to be estimated to a very good approximation for hole transport as half of the splitting of HOMO for different dimers.[64,65] The intermolecular electronic couplings for hole transport in all adjacent dimers were calculated using the M06-2X functional and the cc-pVTZ basis set. Previous benchmarks have shown the ability of the M06-2X functional to describe weak van der Waals interactions for carrier mobility calculations of organic semiconductors.[66,67] Using calculated mobility rates, absolute hole mobilities (μ) can be computed according to the Einstein equation:

$$\mu = \frac{(e \times D)}{(k_B T)} \tag{3}$$

where e is the electronic charge, and D is the diffusion coefficient written as a sum over all the near neighbors in the crystal:

$$D = \frac{1}{2n}\sum_i r^2 W_i P_i \tag{4}$$

In the above equation, n is the dimensionality (3 in our case), r is the distance from the CoM of the representative unit to its ith near neighbor, and P_i corresponds to the probability of hopping between different dimer units:

$$P_i = \frac{W_i}{\sum_i W_i} \tag{5}$$

In-house scripts were developed and used for computational high-throughput screening of λ, V_i, W_i, D, and finally μ for each studied crystal according to the semiclassical Marcus theory discussed above.

2.3. High-Throughput Screening Using the Translational Dimer Model. Various classes of functional groups were chosen to test the effects of bulkiness, polarity, and π-extension on calculated electronic properties and hole mobilities. Guided by the employed procedure to synthesize these materials, the functional groups were substituted in symmetric peripheral positions, as shown in Figure S7. The full list of all functional groups is provided in Figure S8. A modified version of the *chem_tools* code[68] was used to generate the substituted DAT monomers. Other than functionalization, homo and heterocyclic aromatic ring fused π extension was also used to modify DAT. These ring-extended structures are shown in Figure S9.

All generated systems were first optimized using the built-in ETKDG[69] optimizer in the RDkit[70] code. Subsequently, to explore the lowest energy conformers, molecular dynamic simulations were performed at 700 K with a time step of 1.0 fs and a total of 2000 steps with conformers sampled at each time step. For these simulations, the isolated molecule, as obtained from the previous step, was placed at the center of a cubic box with side lengths of at least 25 Å. The semiempirical tight-binding GFN1-xTB[71] method as implemented in CP2K[72] was used for these simulations. The lowest energy conformers were further optimized at the M06L/cc-pVTZ level of theory before calculating the reorganization energies at the M06-2X/cc-pVTZ level, as discussed above.

For DAT, the near neighbor unit is a translational dimer with the CoM distances of 3.9 Å; see Figure S5. Previous studies have indicated that the near neighbor translational dimer units in similar systems exhibit the highest electron transfer integrals.[37,38] Therefore, it can be assumed with a good approximation that the translational dimer constitutes the dominant transport channel, and for accelerated screening, it can be used as a representative of the entire molecular crystal's mobility. Our calculations, as shown in Figure S5, show that using the nearest translational dimer unit in DAT, the calculated hole mobility (0.80 $\text{cm}^2/\text{V}\cdot\text{s}$) closely matches that of the entire crystal (0.73 $\text{cm}^2/\text{V}\cdot\text{s}$) where all adjacent neighbors are considered. Therefore, this shows that the translational dimer model can indeed be employed for high-throughput screening of the electronic coupling and hole mobility of all functionalized DAT systems considered in this work.

To locate the lowest energy dimers of all modified DATs, a comprehensive distance and angle potential energy surface (PES) scan was performed from 3−10 Å with 0.1 Å increments and from 0° to 180° angle with 15° increments, respectively. The GFN1-xTB method was chosen for performing these high-throughput PES scans as an inexpensive and accurate method. GFN-xTB has performed very well in generating accurate structures close to the experiment.[37] For our systems, among different variations of the GFN-xTB methods, the GFN1-xTB variant was found to produce the closest structures to the experiment (see Table S4). For DAT, GFN1-xTB predicted the lowest energy dimer at 3.4 Å, compared to the PBE-MBD lowest energy dimer with a CoM distance of 3.6 Å (Table S4). All screened dimers were then ranked based on their relative energies, with the top 20 isomers selected for calculating averaged electronic couplings, V/λ, and mobilities. Finally, to verify the accuracy of our rankings using the translational dimer model, the crystal structures of the top-performing candidates were predicted, with their carrier mobilities calculated using the semiclassical Marcus theory.

2.4. Crystal Structure Predictions. The crystal structures of DAT, DAS, and the top four novel structures from both functionalized and ring-extended DATs with the highest V/λ values were predicted. First, random crystal structures were generated using the Genarris 2.0 package and a modified CSP

Table 1. Calculated Near Neighbor Center of Mass Distance (CoM), CBM BW, Electron Effective Mass (m_e^*), VBM Bandwidth (VBM BW), Hole Effective Mass (m_h^*), Reorganization Energy (λ) and Hole Mobility (μ) of DAT, DAP, and DAS[a]

Systems	CoM (Å)	CBM BW (eV)	m_e^*	VBM BW (eV)	m_h^*	λ (eV)	μ (cm^2/V·s)
DAT	3.91	0.24	14.01	0.66	4.82	0.30	0.73
DAP	3.80	0.09	52.83	0.11	7.44	0.31	0.11
DAS	8.32	0.06	54.03	0.10	5.33	0.40	0.20

[a] Effective mass is in the unit of electron rest mass m_0.

workflow.[73] Initial structures were generated based on the machine-learned model predicted volume as implemented in Genarris 2.0. During structure generation, the predicted volume was used as the mean volume, but a 6-fold prediction error was used as the standard deviation instead of the 3-fold as implemented in Genarris. This ensured the inclusion of a diverse landscape of initial structures, which were even larger than the structure pools generated in the original Genarris studies.[73,74] For the parent DAS, Z = 8 and Z' = 1 were used, whereas for the parent DAT and its derivatives, Z = 4 and Z' = 1 were used. In every instance the following 26 space groups were considered: $C2$, Cm, Cc, $P2/m$, $P2_1/m$, $P2/c$, $P2_1/c$, $P222$, $P222_1$, $P2_12_12$, $P2_12_12_1$, $Pmm2$, $Pmc2_1$, Pcc_2, $Pma2$, $Pca2_1$, $Pnc2$, $Pmn2_1$, $Pba2$, $Pna2_1$, $Pnn2$, $P4$, $P4_1$, $P4_2$, $P4_3$, and $P\overline{4}$. Next, all generated crystal structures were clustered based on the radial symmetry function (RSF) descriptor and the affinity propagation (AP) machine learning algorithm. Then, they were subjected to dispersion-included PBE-D3 calculations in VASP. All single-point energy calculations in this stage were performed at the Γ point. Later, after selecting the lowest energy structures from each cluster through a second AP clustering, their geometry was optimized by minimizing both atomic positions and cell vectors. PBE-D3 was used for these optimizations, except for the M6 system, for which PBE-MBD was used for more accurate rankings.

In all calculations, the cutoff for plane wave basis sets was set to 500 eV, and a density of at least 0.05 Å^{-1} was employed for the k-point grids. The crystal interaction energies (E_{int}) were calculated as $E_{\text{int}} = (E_{\text{crys}}/n) - E_{\text{mol}}$ where E_{crys} and E_{mol} are calculated total energies of the crystal structure and isolated molecule, respectively, with n corresponding to the number of molecules in the unit cell. Finally, the calculated E_{int} vs densities were analyzed to identify the top candidate crystal structures for each system. Translational motifs within the final predicted crystal structures were identified with an in-house code. To ensure the accuracy of our employed methodology, we performed validation tests for the experimentally reported crystal structure of the parent DAT core[75] as reference. The performance of this validation test is shown in Figure S10, where the experimental structure of DAT was successfully predicted.

3. RESULTS AND DISCUSSION

3.1. Electronic Properties of DAH Cores. PBE-D3 calculated band structure and pDOSs of all studied core DAH materials are given in Figure S4. The DAT and DAS core crystal structures show a direct band gap of 1.3 and 1.0 eV, respectively, whereas DAP illustrates an indirect band gap of 1.5 eV. Based on these computed band gaps, which provide a lower bound to more accurate HSE06 data (1.7 and 2.2 eV for DAT and DAP, respectively), all studied materials can be classified as semiconductors. Using our calculated band structures, the effective masses for holes (m_h^*), which are proportional to the valence band curvature and the valence band maximum (VBM) bandwidth, are calculated (see Table 1). Qualitatively, a less curved band results in a heavier m_h^* leading to a slower charge transport. For DAT, the calculated m_h^*, given in the unit of electron rest mass m_0, is the lowest ($4.82m_0$) compared to DAP and DAS ($7.44m_0$ and $5.33m_0$). Also, a large VBM bandwidth of 0.66 eV is obtained for DAT compared to DAP and DAS, with significantly smaller bandwidths of 0.11 and 0.10 eV, respectively. Analyzing conduction band minimum (CBM) bandwidth and electron effective mass (m_e^*), it was found that m_e^* are significantly higher for all systems compared to m_h^*. As mentioned earlier, a heavier m_e^* illustrates a poorer electron mobility for these systems. Based on our band structure analyses, one can predict qualitatively that the hole mobility of DAT should be higher than the other two systems, making it more suitable as an HTL material.

The band edge alignment of an HTL material with that of the perovskite is an important parameter that can significantly affect the performance of the fabricated PVSC device. Figure 2 presents the PBE-D3 computed vacuum-aligned band edges of the three DAHs compared to those of perovskites. $MAPbI_3$ and $FAPbI_3$ are computed to have similar band gaps of 1.6 eV at the PBE-D3 level, with the latter having a slightly larger ionization potential (IP) of 5.9 eV. Our PBE-D3 computed band gaps agree reasonably well with the reported literature values of 1.55 and 1.48 eV for $MAPbI_3$ and $FAPbI_3$, respectively.[76] Moreover, our calculated higher IP of $FAPbI_3$ agrees with its experimentally observed higher oxidation stability than $MAPbI_3$.[76] Similarly, DAT shows the highest IP of 4.5 eV. Considering the alignment of the band edges with both $MAPbI_3$ and $FAPbI_3$, all studied systems have VBMs that lie above those of the perovskites. This is desirable for the efficient hole migration from the perovskite layer to the HTL material after the photoexcitation. However, for DAT, the VBM aligns better with both $MAPbI_3$ and $FAPbI_3$ than DAP and DAS. Overall, based on our analyses for band edge alignments and IPs, DAT performs better as an HTL material than the other considered systems.

3.2. Hole Mobility of the DAH Cores. The semiclassical Marcus theory is widely used to calculate the carrier mobility in organic semiconductor materials.[77−79] Two important considerations in the Marcus theory are electronic coupling and reorganization energy. The electronic coupling refers to the intermolecular charge transport from one molecule to its near neighbors, while the reorganization energy (λ) refers to the energy penalty associated with geometry relaxations during charge transfer processes. The four-point scheme was used to calculate the reorganization energy of all systems (see the Section 2.2 for more details).[61] DAT is found to have the lowest λ value of 0.30 eV compared to DAP (0.31 eV) and DAS (0.40 eV) (see Table 1). For our systems with herringbone packing motifs, the electronic coupling depends not only on the relative intermolecular CoM distances but also on the orientations of the molecules in the dimers. Considering the calculated couplings between different dimers, DAT has the highest value of 0.21 eV for its near-neighbor translational dimer. On the other hand, the highest computed coupling values for DAP and DAS are 0.06 and 0.09 eV, respectively. Both λ and the electronic coupling determine the overall calculated hole mobilities, although λ carries more importance as it appears in the numerator of the decaying exponential (see the Section 2.2 for more details).

Using the semiclassical Marcus theory, the calculated hole mobility of DAT (0.73 $cm^2/V\cdot s$) was determined to be significantly higher than that of DAP (0.11 $cm^2/V\cdot s$) and DAS (0.20 $cm^2/V\cdot s$) cores (Table 1); see Figure S5 for hole mobility values of DAT in different directions. The enhanced hole mobility for DAT can be attributed to its ordered packing, strong $\pi-\pi$ interactions in the *b* direction, and larger electronic couplings between its near neighbor dimers. Based on the superior properties of DAT as an HTL material, this material was selected for further structural modifications. As mentioned above, different functional groups and π-extensions were considered to decipher useful trends by probing their impacts on the structure and overall calculated electronic properties and hole mobilities.

3.3. Hole Mobilities of the Modified DATs.

Significant efforts are devoted to finding novel organic molecular crystals with high hole mobilities for applications in electronics and optics.[32,43,80,81] Here, an already high hole mobility OMC, i.e., DAT, was considered for further structural modifications. The performance of all functionalized systems is assessed here using two criteria: the ratio of the electronic coupling over λ (V/λ) and the calculated hole mobilities (μ) using the translational dimer model. All the distances between different dimers are the CoM distances. Naturally, the hole mobility will be higher for systems with higher electronic coupling but lower λ. Therefore, the aim here is to maximize electronic coupling values while minimizing λ. One should note that since only the inner reorganization energy is considered here, the computed V/λ ratios and mobilities constitute an overbound to the exact values. Nevertheless, since we are interested in identifying trends, the computed V/λ values offer a valuable and effective screening tool for evaluating the considered systems.

The calculated V/λ ratios and μ for different functional group (FG) substituted DATs and ring-extended DATs are shown in Tables S2 and S3, respectively. Overall, based on the screening metrics, all 74 considered FGs can be classified into four different categories: (i) small sulfur-containing FGs with the highest mobilities, (ii) moderately sized acyclic side groups with unsaturated bonds that give rise to good carrier transport, (iii) halogen-containing FGs exhibiting moderate mobilities, and (iv) bulky alkyl substituents, cyclic or acyclic, that result in poor mobilities. Typically, the electronic coupling exponentially decreases as the molecular separation increases. Hence, the smaller side groups, which do not put a large stress on the core structure, were found to perform better than heavier functional groups. In other words, bulky substituents are more likely to disrupt the inner strain of the DAT core and thus affect electron delocalization across the structure. Although larger in size, side groups containing double or triple bonds were found to produce large electronic couplings. The triple bond containing structures were also found to yield very low λ values, which decrease with the increase in the number of the triple bonds, most likely due to their enhanced ability to accommodate the positive charge. Overall, functional groups with heavy atoms and unsaturated bonds demonstrated a lower bound of λ values, whereas alkyl groups and esters were found to form an upper bound. On the other hand, the ring-extended structures and functional groups with aromatic rings demonstrated a higher value of V due to the π-extension.

The top four best-performing FGs are shown in Figure 3. Overall, three FGs were found to outperform the parent DAT system, including *p*-thiophenyl, thiomethyl, and thiol (see Table S2). Sulfur substituents outperformed other side groups considering both V/λ ratios and hole mobilities. In both cases, three of the top four FGs contain sulfur. Moreover, when ranked by hole mobility, five out of the top ten FGs were found to contain sulfur atoms. Other than sulfur, chlorine and ether-containing FGs were also found to show high hole mobilities. For the ring-extended DAT systems, five out of ten structures outperformed the parent DAT system. The highest-performing structure (M7) and the second-highest (M8) are isomers with perimidine rings in their core. The third (M1) and fifth (M6) structures are π-extended with four extra 6-membered and two extra 5-membered fused aromatic rings. Overall, the effectiveness of π-extension through fused aromatic rings outperformed π-extension through functionalization (compare, for example, M7 to *p*-thiophenyl substituted DAT). We note that the hole mobility of the functionalized DAT systems may be significantly influenced by thermal fluctuations, resulting in anisotropic transport and altered mobilities. To better understand this phenomenon, the calculation of the intermolecular vibrational modes is necessary for each system. However, that would require computationally intensive calculations, and it is therefore beyond the scope of the current study.

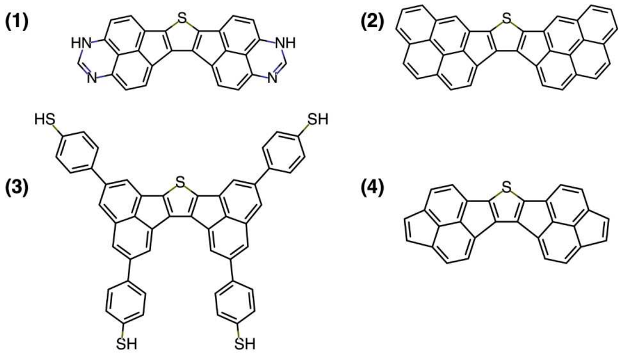

Rank by V/λ	FG / Name	V/λ	μ ($cm^2/V\cdot s$)
1	M7	16.51	72.54
2	M1	6.36	34.61
3	*p*-thiophenyl	2.12	1.03
4	M6	1.61	4.39

Figure 3. Top 4 promising candidates according to the V/λ rankings obtained from applying the translational dimer model.

3.4. Crystal Structure Predictions of the Top-Performing DATs.

Once the V/λ and μ for all functionalized and ring-extended DATs were screened, the structures were ranked to identify the ones with the highest hole mobility. Consequently, four representative systems, including the ring-extended DATs M7, M1, M6, and *p*-thiophenyl substituted DAT were selected for crystal structure predictions based on their high V/λ values

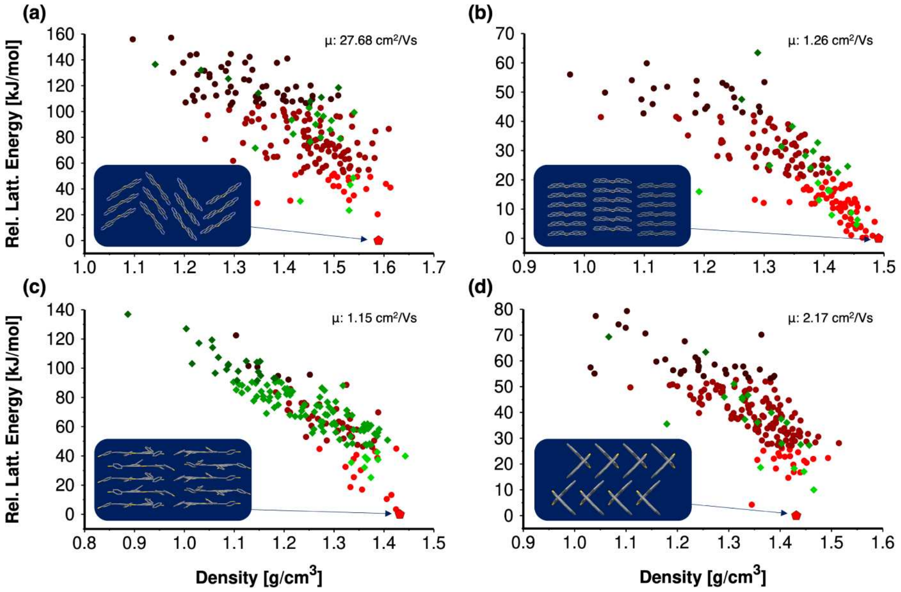

Figure 4. Calculated relative lattice energy vs density correlation plots for (A) M7, (B) M1, (C) *p*-thiophenyl substituted DAT, and (D) M6. PBE-D3 is used in all calculations except for M1, where PBE-MBD is employed. Crystal structures with and without translational dimer motifs are highlighted with red and green colors, respectively, with darker colors representing higher energy polymorphs. Crystal structures of all lowest energy predicted structures are provided as part of the Supporting Information.

(see Figure 3). No solid-state structure has been reported experimentally for these systems, and no carrier mobilities have been reported for them either. As mentioned before, our CSP methodology was first validated using the parent DAT core with an experimentally reported crystal structure. Our methodology correctly predicted the experimental crystal structure of DAT as the lowest energy and highest density structure (see Figure S10). The correlation plots for relative lattice energies vs densities of all four top candidate HTLs are shown in Figure 4. Interestingly, in all four of the lowest energy structures, a columnar packing with the translational dimer motif was found to be present. The lowest energy crystal structures and their calculated hole mobility are shown in the inset. We note that the relatively large relative lattice energy range in our calculated lattice energy vs density plot is due to the adopted workflow where all the candidates shown are the low-energy structures selected from their similarity clusters through AP clustering. As mentioned above, our own validation test for the parent DAT proves the accuracy of this approach for the considered family of OMCs; this method has also been used to successfully predict several other molecular crystals as well.[82,83] In what follows, we provide more details on each of the four predicted crystal structures and their calculated electronic properties and carrier mobilities.

3.4.1. *M7.*

As mentioned above, a columnar packing with the translational dimer motif is present in all lowest energy predicted crystal structures. For M7, the lowest energy structure shows significantly lower energy than the others (Figure 4a). Calculated hole mobility for the whole crystal structure using the semiclassical Marcus theory is 27.68 $\mathrm{cm^2/V{\cdot}s}$ while the predicted hole mobility using only the translational dimer model is 72.54 $\mathrm{cm^2/V{\cdot}s}$ for this system. The CoM distance along the translational dimer is 4.99 Å with an electronic coupling value of 0.02 eV (see Figure 5). As one can intuitively imagine, hydrogen bonds should play a role in the packing of this structure. As shown in Figure 5, hydrogen bonds are formed between the nearby columns. Indeed, because of the formation of these rather strong hydrogen bonds, the predicted structure has a density of 1.59 $\mathrm{g/cm^3}$, which is the highest among all four predicted structures. The building blocks of M7 are two perimidine structures. The core perimidine structure has already been synthesized.[84,85] M7 can, therefore, be an ideal candidate for the synthesis, characterization, and fabrication of PVSCs with high power conversion efficiencies.

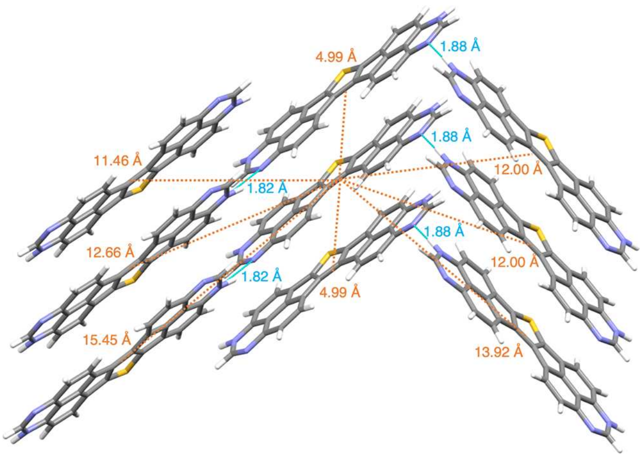

Figure 5. Calculated CoM distances (in orange) between a central molecule and its near neighbor units for the lowest energy crystal structure of M7. The calculated hydrogen bond distances (in blue) are also shown.

3.4.2. *M1.*

Similar to M7, dispersion-corrected PBE-D3 was used for the CSP and final ranking of M1. However, these calculations resulted in multiple low-energy structures with very close energy differences (see Figure S11). To obtain a better resolution for our ranking, PBE-MBD calculations were performed for M1, the results of which are presented in Figure 4b. The translational dimer motif is prevalent throughout the candidate structures, including in the predicted lowest energy one. This structure shows a sheetlike crystal packing. The calculated hole mobility for the predicted crystal structure is 1.26 cm^2/V·s, with a 3.79 Å CoM distance in the translational dimer direction. The CoM distance along the translational direction using the translation dimer model was 3.57 Å. The predicted structure has the lowest energy and the highest density (1.49 g/cm^3, Figure 4b). The extended aromatic rings result in a closely packed π-stacking along the translational direction. The building block of M1, cyclopenta[cd]pyrene, is a well-known polyaromatic hydrocarbon that is already synthesized[86,87] as well.

3.4.3. p-Thiopenyl. p-Thiophenyl substituted DAT has the largest molecular size among the studied four structures. Similar to the rest, the translational dimer motifs are present in the lowest energy structure, although overall, the structures without translational motifs are abundant in the high energy and low-density region (see Figure 4c). Due to the four large side groups, the translational dimer motif was present at a much lower frequency. Calculated hole mobility for the whole crystal structure is 1.15 cm^2/V·s, which is >50% higher than the parent DAT (0.73 cm^2/V·s). The CoM distance along the translational direction for the predicted structure is 4.75 Å with a coupling value of 0.10 eV. Translational dimers are slipped to accommodate the bulky p-thiophenyl groups, forming a slipped sheetlike packing motif. The second lowest energy structure in the correlation plot has an energy difference of 13.9 kJ/mol from the lowest energy structure. It forms a sheetlike packing as well, but more slipped compared to the lowest energy structure (see Figure S12). As a result, it demonstrates a higher overlap and a higher coupling between near neighbors, resulting in a hole mobility value of 2.08 cm^2/V·s. *tert*-Butyl functionalized DAT with a similar substitution pattern as demonstrated in this work has been synthesized before.[24] A similar synthetic approach can be adopted for synthesizing p-thiophenyl substituted DAT.

3.4.4. M6. M6 is the smallest monomer of all four, containing two 5-membered aromatic rings fused to the DAT core structure. As shown in Figure 4d, the translational dimer motifs are prominent in most of the M6 crystal structures. Similar to the others, the lowest energy structure has a translational dimer motif with a full eclipse pattern and a hole mobility of 2.17 cm^2/V·s. It forms a herringbone crystal packing with a CoM distance of 4.72 Å in between dimers in the translational direction. The reorganization energy for M6 is the highest (0.22 eV) among all four structures. However, the relatively large electronic coupling compensates for this. The building unit of M6, cyclopent[fg]acenaphthylene, has also been synthesized before.[88] Similar to the other three, this structure is also expected to be synthetically viable. In addition to mobilities, the band edge alignments of all four predicted structures were calculated relative to $MAPbI_3$ and $FAPbI_3$ perovskites, where all showed good alignments similar to the DAT core (see Figure S13).

Finally, the calculated hole mobilities along different dimers in the M7 structure with the highest overall calculated hole mobility is tabulated in Figure S14. Interestingly, it was found that the translational dimer no longer contributes as the main hole-transporting channel for this system, and rather, the dimer with explicit peripheral hydrogen bonds illustrates the highest calculated hole mobility among all dimers (see Figure 5). We, therefore, caution against the generalizability and use of the translational dimer approach for high-throughput screening of different molecular crystals before detailed benchmarks. This is especially important in cases where there are explicit and comparatively strong interactions other than π–π stacking between the molecules, such as hydrogen bonds in M7. As one of the limitations of our study, the semiclassical Marcus theory used here for describing the charge transfer mechanism neglects dynamic disorder originating from thermal fluctuations. In the hopping regime of the Marcus theory, the intermolecular electronic coupling is kept fixed. However, at room temperature, because of the weak van der Waals interactions in organic molecular crystals, the orientation of the molecule will fluctuate continuously as the charge transfer integral is modulated by nuclear motions. There are several approaches to include the dynamic disorder. For example, a phonon-assisted term can be added to the temperature dependence of mobility. Nevertheless, despite its limitations, the Marcus theory has been widely used to describe the charge transfer mechanism in various organic molecular crystals at room temperature and has shown good agreement with experiments.

4. CONCLUSIONS

Of the 3 DAH structures, the unfunctionalized DAT core was found to exhibit the highest hole mobility. This correlated well with its calculated low hole effective mass, large VBM bandwidth, and low reorganization energy. Moreover, the VBM of DAT was found to align better with common perovskite materials such as $MAPbI_3$ and $FAPbI_3$. Using the translational dimer model, high-throughput screening calculations were performed for a total of 74 structurally modified DATs with different functional groups and π-extended systems. Those structures with higher hole mobilities than the parent DAT were selected for crystal structure predictions, which validated the accuracy of using the translational dimer model for high throughput screening. The lowest energy polymorphs of the 4 predicted crystal structures from CSP yielded higher hole mobilities than the parent DAT, with the translational dimer motifs consistently found to be present in the predicted structures. This study provides useful insights into different factors contributing to high carrier mobilities in OMCs. In addition to extending the π-conjugation, the presence of heterocycles, functional groups such as sulfur atoms, and their orientations are also found to play crucial roles in carrier mobilities. Our results provide a clearer picture of the hole mobility mechanism in OMCs and offer useful insights for fast theoretical high-throughput screening and the inverse design of OMCs with high mobilities. Future works will involve the inclusion of dynamic disorder for further improvement of the calculated mobilities in OMCs.

■ ASSOCIATED CONTENT

Supporting Information

The Supporting Information is available free of charge at https://pubs.acs.org/doi/10.1021/acs.cgd.4c00965.

> Details of our calculations, including correlation plot for the CSP predicted crystal structure of DAS and the comparison of its properties to the experimental structure, the benchmark of different XC functionals, k-point paths for all DAHs, band structures and projected density of states of different DAHs, crystal structures of perovskites, different functionalized DATs, V/λ and hole mobility values of all 74 functionalized DATs, the list of mobilities of all translational dimers for DAT, CSP validation (PBE-D3) for the parent DAT,

PBE-D3 calculated relative lattice energy vs density correlation plot for M1, PBE-D3 predicted second-ranked crystal structure of the *p*-thiophenyl functionalized DAT, vacuum-aligned band edges for the top functionalized systems (PDF)

XYZ coordinates of different DAT core dimers (ZIP)

Crystallographic information files of all top functionalized systems (ZIP)

AUTHOR INFORMATION

Corresponding Authors

Zhonghua Peng − *Division of Energy, Matter and Systems, School of Science and Engineering, University of Missouri − Kansas City, Kansas City, Missouri 64110, United States*; Email: pengz@umkc.edu

Mohammad R. Momeni − *Division of Energy, Matter and Systems, School of Science and Engineering, University of Missouri − Kansas City, Kansas City, Missouri 64110, United States*; orcid.org/0000-0002-7731-5823; Email: mmomenitaheri@umkc.edu

Authors

Md Omar Faruque − *Division of Energy, Matter and Systems, School of Science and Engineering, University of Missouri − Kansas City, Kansas City, Missouri 64110, United States*

Suchona Akter − *Division of Energy, Matter and Systems, School of Science and Engineering, University of Missouri − Kansas City, Kansas City, Missouri 64110, United States*

Dil K. Limbu − *Division of Energy, Matter and Systems, School of Science and Engineering, University of Missouri − Kansas City, Kansas City, Missouri 64110, United States*; orcid.org/0000-0001-9196-9498

Kathleen V. Kilway − *Division of Energy, Matter and Systems, School of Science and Engineering, University of Missouri − Kansas City, Kansas City, Missouri 64110, United States*

Complete contact information is available at: https://pubs.acs.org/10.1021/acs.cgd.4c00965

Notes

The authors declare no competing financial interest.

ACKNOWLEDGMENTS

This research was supported by the National Science Foundation through award no. DMR-2308895. Simulations used resources from Bridges-2[89] at Pittsburgh Supercomputing Center through allocation CHE200007, CHE200008, and PHY230099 from the Advanced Cyberinfrastructure Coordination Ecosystem: Services & Support (ACCESS) program,[90] which is supported by National Science Foundation grants #2138259, #2138286, #2138307, #2137603, and #2138296. Technical support and computing resources provided by the HPC center at UMKC are also gratefully acknowledged.

REFERENCES

(1) Kojima, A.; Teshima, K.; Shirai, Y.; Miyasaka, T. Organometal Halide Perovskites as Visible-Light Sensitizers for Photovoltaic Cells. *J. Am. Chem. Soc.* **2009**, *131*, 6050−6051.

(2) Lee, M. M.; Teuscher, J.; Miyasaka, T.; Murakami, T. N.; Snaith, H. J. Efficient hybrid solar cells based on meso-superstructured organometal halide perovskites. *Science* **2012**, *338*, 643−647.

(3) Jeon, N. J.; Noh, J. H.; Yang, W. S.; Kim, Y. C.; Ryu, S.; Seo, J.; Seok, S. I. Compositional engineering of perovskite materials for high-performance solar cells. *Nature* **2015**, *517*, 476−480.

(4) Yang, W. S.; Noh, J. H.; Jeon, N. J.; Kim, Y. C.; Ryu, S.; Seo, J.; Seok, S. I. High-performance photovoltaic perovskite layers fabricated through intramolecular exchange. *Science* **2015**, *348*, 1234−1237.

(5) Chen, W.; Wu, Y.; Yue, Y.; Liu, J.; Zhang, W.; Yang, X.; Chen, H.; Bi, E.; Ashraful, I.; Grätzel, M.; Han, L. Efficient and stable large-area perovskite solar cells with inorganic charge extraction layers. *Science* **2015**, *350*, 944−948.

(6) Li, X.; Bi, D.; Yi, C.; Décoppet, J.-D.; Luo, J.; Zakeeruddin, S. M.; Hagfeldt, A.; Grätzel, M. A vacuum flash−assisted solution process for high-efficiency large-area perovskite solar cells. *Science* **2016**, *353*, 58−62.

(7) Arora, N.; Dar, M. I.; Hinderhofer, A.; Pellet, N.; Schreiber, F.; Zakeeruddin, S. M.; Grätzel, M. Perovskite Solar Cells With CuSCN Hole Extraction Layers Yield Stabilized Efficiencies Greater Than 20%. *Science* **2017**, *358*, 768−771.

(8) Yang, W. S.; Park, B.-W.; Jung, E. H.; Jeon, N. J.; Kim, Y. C.; Lee, D. U.; Shin, S. S.; Seo, J.; Kim, E. K.; Noh, J. H.; Seok, S. I. Iodide management in formamidinium-lead-halide−based perovskite layers for efficient solar cells. *Science* **2017**, *356*, 1376−1379.

(9) Jeon, N. J.; Na, H.; Jung, E. H.; Yang, T.-Y.; Lee, Y. G.; Kim, G.; Shin, H.-W.; Il Seok, S.; Lee, J.; Seo, J. A fluorene-terminated hole-transporting material for highly efficient and stable perovskite solar cells. *Nat. Energy* **2018**, *3*, 682−689.

(10) Min, H.; Lee, D. Y.; Kim, J.; Kim, G.; Lee, K. S.; Kim, J.; Paik, M. J.; Kim, Y. K.; Kim, K. S.; Kim, M. G.; Shin, T. J.; Seok, S. I. Perovskite solar cells with atomically coherent interlayers on SnO2 electrodes. *Nature* **2021**, *598*, 444−450.

(11) Green, M. A.; Hishikawa, Y.; Dunlop, E.; Levi, D.; Hohl-Ebinger, J.; Yoshita, M.; Ho-Baillie, A. Solar cell efficiency tables (version 53) Progress in Photovoltaics. *Res. Appl.* **2019**, *27*, 3−12.

(12) Gratia, P.; Magomedov, A.; Malinauskas, T.; Daskeviciene, M.; Abate, A.; Ahmad, S.; Grätzel, M.; Getautis, V.; Nazeeruddin, M. K. A methoxydiphenylamine-substituted carbazole twin derivative: an efficient hole-transporting material for perovskite solar cells. *Angew. Chem., Int. Ed.* **2015**, *54*, 11409−11413.

(13) Huang, C.; Fu, W.; Li, C.-Z.; Zhang, Z.; Qiu, W.; Shi, M.; Heremans, P.; Jen, A. K.-Y.; Chen, H. Dopant-free hole-transporting material with a C 3 h symmetrical truxene core for highly efficient perovskite solar cells. *J. Am. Chem. Soc.* **2016**, *138*, 2528−2531.

(14) Lee, J.; Malekshahi Byranvand, M.; Kang, G.; Son, S. Y.; Song, S.; Kim, G.-W.; Park, T. Green-solvent-processable, dopant-free hole-transporting materials for robust and efficient perovskite solar cells. *J. Am. Chem. Soc.* **2017**, *139*, 12175−12181.

(15) Kim, Y. C.; Yang, T.-Y.; Jeon, N.; Im, J.; Jang, S.; Shin, T.; Shin, H.-W.; Kim, S.; Lee, E.; Kim, S.; Noh, J. H.; Seok, S. I.; Seo, J. Engineering interface structures between lead halide perovskite and copper phthalocyanine for efficient and stable perovskite solar cells. *Energy Environ. Sci.* **2017**, *10*, 2109−2116.

(16) Park, S.; Heo, J. H.; Cheon, C. H.; Kim, H.; Im, S. H.; Son, H. J. A [2, 2] paracyclophane triarylamine-based hole-transporting material for high performance perovskite solar cells. *J. Mater. Chem. A* **2015**, *3*, 24215−24220.

(17) Bi, D.; Mishra, A.; Gao, P.; Franckevičius, M.; Steck, C.; Zakeeruddin, S. M.; Nazeeruddin, M. K.; Bäuerle, P.; Grätzel, M.; Hagfeldt, A. High-Efficiency Perovskite Solar Cells Employing a S, N-Heteropentacene-based D−A Hole-Transport Material. *ChemSuschem* **2016**, *9*, 433−438.

(18) Calió, L.; Kazim, S.; Grätzel, M.; Ahmad, S. Hole-transport materials for perovskite solar cells. *Angew. Chem., Int. Ed.* **2016**, *55*, 14522−14545.

(19) Kim, J. Y.; Lee, J.-W.; Jung, H. S.; Shin, H.; Park, N.-G. High-efficiency perovskite solar cells. *Chem. Rev.* **2020**, *120*, 7867−7918.

(20) Bakr, Z. H.; Wali, Q.; Fakharuddin, A.; Schmidt-Mende, L.; Brown, T. M.; Jose, R. Advances in Hole Transport Materials Engineering for Stable and Efficient Perovskite Solar Cells. *Nano Energy* **2017**, *34*, 271−305.

(21) Pham, H. D.; Yang, T. C.-J.; Jain, S. M.; Wilson, G. J.; Sonar, P. Development of dopant-free organic hole transporting materials for perovskite solar cells. *Adv. Energy Mater.* **2020**, *10*, 1903326.

(22) Urieta-Mora, J.; García-Benito, I.; Molina-Ontoria, A.; Martín, N. Hole transporting materials for perovskite solar cells: a chemical approach. *Chem. Soc. Rev.* **2018**, *47*, 8541−8571.

(23) Singh, R.; Singh, P. K.; Bhattacharya, B.; Rhee, H.-W. Review of current progress in inorganic hole-transport materials for perovskite solar cells. *Appl. Mater. Today* **2019**, *14*, 175−200.

(24) Li, Y.; Scheel, K. R.; Clevenger, R. G.; Shou, W.; Pan, H.; Kilway, K. V.; Peng, Z. Highly Efficient and Stable Perovskite Solar Cells Using a Dopant-Free Inexpensive Small Molecule as the Hole-Transporting Material. *Adv. Energy Mater.* **2018**, *8*, 1801248.

(25) Li, Y.; Clevenger, R. G.; Jin, L.; Kilway, K. V.; Peng, Z. Unusually high SCLC hole mobility in solution-processed thin films of a polycyclic thiophene-based small-molecule semiconductor. *J. Mater. Chem. C* **2014**, *2*, 7180−7183.

(26) Li, Y.; Clevenger, R. G.; Jin, L.; Kilway, K. V.; Peng, Z. Spin-coated thin films of polycyclic aromatic hydrocarbons exhibiting high SCLC hole mobilities. *J. Phys. Chem. C* **2016**, *120*, 841−852.

(27) Sundar, V. C.; Zaumseil, J.; Podzorov, V.; Menard, E.; Willett, R. L.; Someya, T.; Gershenson, M. E.; Rogers, J. A. Elastomeric Transistor Stamps: Reversible Probing of Charge Transport in Organic Crystals. *Science* **2004**, *303*, 1644−1646.

(28) Podzorov, V.; Menard, E.; Borissov, A.; Kiryukhin, V.; Rogers, J. A.; Gershenson, M. E. Intrinsic Charge Transport on the Surface of Organic Semiconductors. *Phys. Rev. Lett.* **2004**, *93*, 086602.

(29) Tang, C. W.; VanSlyke, S. A. Organic electroluminescent diodes. *Appl. Phys. Lett.* **1987**, *51*, 913−915.

(30) Chamberlain, G. Organic solar cells: A review. *Sol. Cells* **1983**, *8*, 47−83.

(31) Kalb, W. L.; Mattenberger, K.; Batlogg, B. Oxygen-related traps in pentacene thin films: Energetic position and implications for transistor performance. *Phys. Rev. B* **2008**, *78*, 035334.

(32) Nguyen, T. P.; Shim, J. H.; Lee, J. Y. Density functional theory studies of hole mobility in picene and pentacene crystals. *J. Phys. Chem. C* **2015**, *119*, 11301−11310.

(33) Dong, S.; Ong, A.; Chi, C. Photochemistry of various acene based molecules. *J. Photochem. Photobiol., C* **2019**, *38*, 27−46.

(34) Clapp, D. B. The reaction of a thiophene derivative with maleic anhydride. *J. Am. Chem. Soc.* **1939**, *61*, 2733−2735.

(35) Nagasaka, Y.; Kitamura, C.; Kurata, H.; Kawase, T. Diacenaphtho [1, 2,b; 1, 2-d] silole and-pyrrole. *Chem. Lett.* **2011**, *40*, 1437−1439.

(36) Adams, R. D.; Captain, B.; Smith Jr, J. L. Diacenaphtho [1, 2-c: 1, 2-e]-1, 2-dithiin: Synthesis, Structure and Reactivity. *J. Organomet. Chem.* **2004**, *689*, 65−70.

(37) Schmidt, J. A.; Weatherby, J. A.; Sugden, I. J.; Santana-Bonilla, A.; Salerno, F.; Fuchter, M. J.; Johnson, E. R.; Nelson, J.; Jelfs, K. E. Computational screening of chiral organic semiconductors: exploring side-group functionalization and assembly to optimize charge transport. *Cryst. Growth Des.* **2021**, *21*, 5036−5049.

(38) Salerno, F.; Rice, B.; Schmidt, J. A.; Fuchter, M. J.; Nelson, J.; Jelfs, K. E. The influence of nitrogen position on charge carrier mobility in enantiopure aza [6] helicene crystals. *Phys. Chem. Chem. Phys.* **2019**, *21*, 5059−5067.

(39) Rossi, M.; Sohlberg, K. Predictions of Hole Mobility in Molecular Organic Crystals: Incorporating Thermal Effects. *J. Phys. Chem. C* **2009**, *113*, 6821−6831.

(40) Park, J. W.; Lee, K. I.; Choi, Y.-S.; Kim, J.-H.; Jeong, D.; Kwon, Y.-N.; Park, J.-B.; Ahn, H. Y.; Park, J.-I.; Lee, H. S.; Shin, J. The prediction of hole mobility in organic semiconductors and its calibration based on the grain-boundary effect. *Phys. Chem. Chem. Phys.* **2016**, *18*, 21371−21380.

(41) Krawczuk, R. A.; Tierney, S.; Mitchell, W.; McDouall, J. J. W. Computational investigation of hole mobilities in organic semiconductors: comparison of single crystal structures and surface adsorbed clusters. *Faraday Discuss.* **2014**, *174*, 281−296.

(42) Deng, W.-Q.; Goddard, W. A. Predictions of hole mobilities in oligoacene organic semiconductors from quantum mechanical calculations. *J. Phys. Chem. B* **2004**, *108*, 8614−8621.

(43) Sokolov, A. N.; Atahan-Evrenk, S.; Mondal, R.; Akkerman, H. B.; Sánchez-Carrera, R. S.; Granados-Focil, S.; Schrier, J.; Mannsfeld, S. C.; Zoombelt, A. P.; Bao, Z.; Aspuru-Guzik, A. From computational discovery to experimental characterization of a high hole mobility organic crystal. *Nat. Commun.* **2011**, *2*, 437.

(44) Troisi, A.; Orlandi, G. Band Structure of the Four Pentacene Polymorphs and Effect on the Hole Mobility at Low Temperature. *J. Phys. Chem. B* **2005**, *109*, 1849−1856.

(45) Zeng, H.-P.; OuYang, X.-H.; Wang, T.-T.; Yuan, G.-Z.; Zhang, G.-H.; Zhang, X.-M. Synthesis, Crystal Structure, and Prediction of Hole Mobilities of 2,7′-Ethylenebis(8-hydroxyquinoline). *Cryst. Growth Des.* **2006**, *6*, 1697−1702.

(46) Kresse, G.; Hafner, J. Ab initio molecular dynamics for liquid metals. *Phys. Rev. B* **1993**, *47*, 558−561.

(47) Kresse, G.; Hafner, J. Ab initio molecular-dynamics simulation of the liquid-metal−amorphous-semiconductor transition in germanium. *Phys. Rev. B* **1994**, *49*, 14251−14269.

(48) Kresse, G.; Furthmüller, J. Efficiency of ab-initio total energy calculations for metals and semiconductors using a plane-wave basis set. *Comput. Mater. Sci.* **1996**, *6*, 15−50.

(49) Kresse, G.; Furthmüller, J. Efficient iterative schemes for ab initio total-energy calculations using a plane-wave basis set. *Phys. Rev. B* **1996**, *54*, 11169−11186.

(50) Perdew, J. P.; Burke, K.; Ernzerhof, M. Erratum: Generalized gradient approximation made simple. *Phys. Rev. Lett.* **1997**, *78*, 1396−1396.

(51) Hammer, B.; Hansen, L. B.; Nørskov, J. K. Improved adsorption energetics within density-functional theory using revised Perdew-Burke-Ernzerhof functionals. *Phys. Rev. B* **1999**, *59*, 7413−7421.

(52) Perdew, J. P.; Ruzsinszky, A.; Csonka, G. I.; Vydrov, O. A.; Scuseria, G. E.; Constantin, L. A.; Zhou, X.; Burke, K. Restoring the Density-Gradient Expansion for Exchange in Solids and Surfaces. *Phys. Rev. Lett.* **2008**, *100*, 136406.

(53) Grimme, S.; Antony, J.; Ehrlich, S.; Krieg, H. A consistent and accurate ab initio parametrization of density functional dispersion correction (DFT-D) for the 94 elements H-Pu. *J. Chem. Phys.* **2010**, *132* (15), 154104.

(54) Tkatchenko, A.; Scheffler, M. Accurate molecular van der Waals interactions from ground-state electron density and free-atom reference data. *Phys. Rev. Lett.* **2009**, *102*, 073005.

(55) Ambrosetti, A.; Reilly, A. M.; DiStasio, R. A.; Tkatchenko, A. Long-range Correlation Energy Calculated From Coupled Atomic Response Functions. *J. Chem. Phys.* **2014**, *140* (18), 18A508.

(56) Tkatchenko, A.; DiStasio, R. A.; Car, R.; Scheffler, M. Accurate and efficient method for many-body van der Waals interactions. *Phys. Rev. Lett.* **2012**, *108* (23), 236402.

(57) Blöchl, P. E. Projector augmented-wave method. *Phys. Rev. B* **1994**, *50*, 17953−17979.

(58) Kresse, G.; Joubert, D. From ultrasoft pseudopotentials to the projector augmented-wave method. *Phys. Rev. B* **1999**, *59*, 1758−1775.

(59) Sholl, D. S.; Steckel, J. A. *Density Functional Theory: A Practical Introduction*; John Wiley & Sons, 2011.

(60) Walsh, A. Principles of chemical bonding and band gap engineering in hybrid organic−inorganic halide perovskites. *J. Phys. Chem. C* **2015**, *119*, 5755−5760.

(61) Dell'angelo, D.; Momeni, M. R.; Pearson, S.; Shakib, F. A. Modeling energy transfer and absorption spectra in layered metal−organic frameworks based on a Frenkel−Holstein Hamiltonian. *J. Chem. Phys.* **2022**, *156*, 044109.

(62) Frisch, M. J.; Trucks, G. W.; Schlegel, H. B.; Scuseria, G. E.; Robb, M. A.; Cheeseman, J. R.; Scalmani, G.; Barone, V.; Petersson, G. A.; Nakatsuji, H. et al. *Gaussian 16 Revision C.01.*; Gaussian Inc: Wallingford CT, 2016.

(63) Ostroverkhova, O. *Handbook of Organic Materials for Optical and (Opto) Electronic Devices: properties and Applications*; Elsevier, 2013.

(64) Cornil, J.; Beljonne, D.; Calbert, J.-P.; Brédas, J.-L. Interchain interactions in organic π-conjugated materials: impact on electronic structure, optical response, and charge transport. *Adv. Mater.* **2001**, *13*, 1053−1067.

(65) Kashimoto, Y.; Yonezawa, K.; Meissner, M.; Gruenewald, M.; Ueba, T.; Kera, S.; Forker, R.; Fritz, T.; Yoshida, H. The evolution of intermolecular energy bands of occupied and unoccupied molecular states in organic thin films. *J. Phys. Chem. C* **2018**, *122*, 12090−12097.

(66) Wheeler, S. E. Understanding Substituent Effects in Noncovalent Interactions Involving Aromatic Rings. *Acc. Chem. Res.* **2013**, *46*, 1029−1038.

(67) Calvo-Castro, J.; Warzecha, M.; Kennedy, A. R.; McHugh, C. J.; McLean, A. J. Impact of Systematic Structural Variation on the Energetics of π−π Stacking Interactions and Associated Computed Charge Transfer Integrals of Crystalline Diketopyrrolopyrroles. *Cryst. Growth Des.* **2014**, *14*, 4849−4858.

(68) Turcani, L. *lukasturcani/chem_tools*. 2020; https://github.com/lukasturcani/chem_tools.

(69) Riniker, S.; Landrum, G. A. Better informed distance geometry: using what we know to improve conformation generation. *J. Chem. Inf. Model.* **2015**, *55*, 2562−2574.

(70) *RDKit: Open-Source Cheminformatics Software* https://www.rdkit.org/.

(71) Grimme, S.; Bannwarth, C.; Shushkov, P. A robust and accurate tight-binding quantum chemical method for structures, vibrational frequencies, and noncovalent interactions of large molecular systems parametrized for all spd-block elements (Z= 1−86). *J. Chem. Theory Comput.* **2017**, *13*, 1989−2009.

(72) Kühne, T. D.; Iannuzzi, M.; Del Ben, M.; Rybkin, V. V.; Seewald, P.; Stein, F.; Laino, T.; Khaliullin, R. Z.; Schütt, O.; Schiffmann, F. CP2K: An electronic structure and molecular dynamics software package-Quickstep: Efficient and accurate electronic structure calculations. *J. Chem. Phys.* **2020**, *152*, 194103.

(73) Tom, R.; Rose, T.; Bier, I.; O'Brien, H.; Vázquez-Mayagoitia, Á.; Marom, N. Genarris 2.0: A random structure generator for molecular crystals. *Comput. Phys. Commun.* **2020**, *250*, 107170.

(74) Li, X.; Curtis, F. S.; Rose, T.; Schober, C.; Vazquez-Mayagoitia, A.; Reuter, K.; Oberhofer, H.; Marom, N. Genarris: Random generation of molecular crystal structures and fast screening with a Harris approximation. *J. Chem. Phys.* **2018**, *148* (24), 241701.

(75) Musgrave, O. C.; Skakle, J. M. Diacenaphtheno [7, 8-b: 71, 81-d] thiophene. *Acta Crystallogr. Sect. E: struct. Rep.* **2004**, *60*, o359−o360.

(76) Zheng, Z.; Wang, S.; Hu, Y.; Rong, Y.; Mei, A.; Han, H. Development of formamidinium lead iodide-based perovskite solar cells: efficiency and stability. *Chem. Sci.* **2022**, *13*, 2167−2183.

(77) Zhang, X.-Y.; Huang, J.-D.; Yu, J.-J.; Li, P.; Zhang, W.-P.; Frauenheim, T. Anisotropic electron-transfer mobilities in diethynylindenofluorene-dione crystals as high-performance n-type organic semiconductor materials: remarkable enhancement by varying substituents. *Phys. Chem. Chem. Phys.* **2015**, *17*, 25463−25470.

(78) Yuan, J.; Jiang, H.; Yang, Q.; Xiang, Y.; Zhang, Y.; Dai, Y.; Li, P.; Zheng, C.; Xie, G.; Chen, R. A solution-processable wholly-aromatic bipolar host material for highly efficient blue electroluminescent devices. *J. Mater. Chem. C* **2021**, *9*, 687−692.

(79) Zhang, S.; Talnack, F.; Jousselin-Oba, T.; Bhat, V.; Wu, Y.; Lei, Y.; Tomo, Y.; Gong, H.; Michalek, L.; Zhong, D. Shear-aligned large-area organic semiconductor crystals through extended π-π interaction. *J. Mater. Chem. C* **2023**, *11*, 8992−9001.

(80) Nakata, H.; Kitoh-Nishioka, H.; Sakai, W.; Choi, C. H. Toward Accurate Prediction of Ion Mobility in Organic Semiconductors by Atomistic Simulation. *J. Chem. Theory Comput.* **2023**, *19*, 1517−1528.

(81) Nguyen, T. P.; Roy, P.; Shim, J. H. Remarkable charge-transfer mobility from [6] to [10] phenacene as a high performance p-type organic semiconductor. *Phys. Chem. Chem. Phys.* **2018**, *20*, 8658−8667.

(82) Bier, I.; O'Connor, D.; Hsieh, Y.-T.; Wen, W.; Hiszpanski, A. M.; Han, T. Y.-J.; Marom, N. Crystal structure prediction of energetic materials and a twisted arene with Genarris and GAtor. *CrystEngcomm* **2021**, *23*, 6023−6038.

(83) O'Connor, D.; Bier, I.; Tom, R.; Hiszpanski, A. M.; Steele, B. A.; Marom, N. Ab Initio Crystal Structure Prediction of the Energetic Materials LLM-105, RDX, and HMX. *Cryst. Growth Des.* **2023**, *23*, 6275−6289.

(84) Pozharskii, A. F.; Gulevskaya, A. V.; Claramunt, R. M.; Alkorta, I.; Elguero, J. Perimidines: a unique π-amphoteric heteroaromatic system. *Russ. Chem. Rev.* **2020**, *89*, 1204.

(85) Rewcastle, G. Pyrimidines and their benzo derivatives. In *Comprehensive Heterocyclic Chemistry III*; Elsevier, 2008.

(86) Konieczny, M.; Harvey, R. G. Synthesis of cyclopenta [cd] pyrene. *J. Org. Chem.* **1979**, *44*, 2158−2160.

(87) Murray, R. W.; Singh, M. Quantitative synthesis and formation of cyclopenta [cd] pyrene 3, 4-oxide under simulated atmospheric conditions. *Chem. Res. Toxicol.* **1995**, *8*, 239−243.

(88) Siegel, J. S.; Tobe, Y.; Shinkai, I. *Category 6, Compounds with All-Carbon Functions: aromatic Ring Assemblies, Polycyclic Aromatic Hydrocarbons, and Conjugated Polyenes*; Georg Thieme Verlag: Stuttgart, 2009.

(89) Brown, S. T.; Buitrago, P.; Hanna, E.; Sanielevici, S.; Scibek, R.; Nystrom, N. A. A platform for rapidly-evolving and data intensive research. *Practice And Experience In Advanced Research Computing*; ACM, 2021, 14.

(90) Boerner, T. J.; Deems, S.; Furlani, T. R.; Knuth, S. L.; Towns, J. ACCESS: Advancing Innovation: NSF's Advanced Cyberinfrastructure Coordination Ecosystem: Services & Support. *Practice And Experience In Advanced Research Computing*; ACM, 2023, 173176.